

**This item is the archived peer-reviewed author-version of:**

Effect of hydriding induced defects on the small-scale plasticity mechanisms in nanocrystalline palladium thin films

**Reference:**

Lumbeeck Gunnar, Idrissi Hosni, Amin-Ahmadi Behnam, Favache Audrey, Delmelle Renaud, Samaeeaghmiyoni Vahid, Proost Joris, Pardoen Thomas, Schryvers Dominique.- Effect of hydriding induced defects on the small-scale plasticity mechanisms in nanocrystalline palladium thin films  
Journal of applied physics / American Institute of Physics - ISSN 1089-7550 - 124:22(2018), 225105  
Full text (Publisher's DOI): <https://doi.org/10.1063/1.5055274>

# Effect of hydriding induced defects on the small-scale plasticity mechanisms in nanocrystalline palladium thin films

Gunnar Lumbeeck<sup>1</sup>, Hosni Idrissi<sup>2,1</sup>, Behnam Amin-Ahmadi<sup>3</sup>, Audrey Favache<sup>2</sup>, Renaud Delmelle<sup>4</sup>, Vahid Samaee<sup>1</sup>, Joris Proost<sup>2</sup>, Thomas Pardoën<sup>2</sup>, Dominique Schryvers<sup>1</sup>

<sup>1</sup>Electron Microscopy for Materials Science (EMAT), Department of Physics, University of Antwerp, Groenenborgerlaan 171, B-2020 Antwerp, Belgium

<sup>2</sup>Institute of Mechanics, Materials and Civil Engineering, UCLouvain, Place Sainte Barbe 2, B-1348 Louvain-la-Neuve, Belgium

<sup>3</sup>Department of mechanical Engineering, Colorado School of Mines, 1500 Illinois St, Golden, CO 80401, USA

<sup>4</sup>Institute for Materials and Process Engineering (IMPE), Zurich University of Applied Sciences, Technikumstrasse 9, 8400 Winterthur, Switzerland

## Abstract

Nanoindentation tests performed on nanocrystalline palladium films subjected to hydriding/dehydriding cycles demonstrate significant softening when compared to the as-received material. The origin of this softening is unraveled by combining in-situ TEM nanomechanical testing with automated crystal orientation mapping in TEM and high resolution TEM. The softening is attributed to the presence of a high density of stacking faults and of Shockley partial dislocations after hydrogen loading. The hydrogen induced defects affect the elementary plasticity mechanisms and the mechanical response by acting as preferential sites for twinning/detwinning during deformation. These results are analyzed and compared to previous experimental and simulation works in the literature. This study provides new insights on the effect of hydrogen on the atomistic deformation and cracking mechanisms as well as on the mechanical properties of nanocrystalline thin films and membranes.

## Keywords

Nanocrystalline Pd films, Mechanical testing, ACOM-TEM, Stacking faults, Electron microscopy

## I. Introduction

Owing to its fast and reversible hydriding kinetics, palladium (Pd) is an ideal model system to study the effect of hydrogen (H) absorption. This is essential for hydrogen energy technology, one of the cleanest alternatives to fossil fuels as well as for purification and sensing applications. Pd has a high sensitivity and selectivity with respect to hydrogen and can release hydrogen at room temperature<sup>1,2</sup>. Recently, nanocrystalline (nc) Pd thin films have been widely used in hydrogen applications because of large surface and subsurface site densities and of the presence of a high fraction of grain boundaries (GBs) which can facilitate

45 the hydriding process<sup>3,4</sup>. However, these layers must be thin enough to ensure high  
46 hydrogen permeability while remaining mechanically sound and sufficiently ductile<sup>5,6</sup>.

47

48 The crystalline structure of Pd is face centered cubic (fcc), also referred to as the  $\alpha$ -phase.  
49 Interstitial hydrogen atoms occupy part of the octahedral sites of the  $\alpha$ -phase. During  
50 hydriding, as long as the H/Pd ratio stays below  $\alpha_{SSmax} \sim 0.02$  (atomic ratio) at room  
51 temperature, the fcc  $\alpha$ -Pd lattice parameter can expand from 3.889 Å to 3.895 Å. When the  
52 H/Pd ratio reaches 0.02, the so-called  $\beta$ -phase appears with a lattice constant near 4.025 Å.  
53 The  $\beta$ -phase exhibits an fcc structure as well. The two phases coexist up to a ratio H/Pd  $\beta_{SSmin}$   
54  $\sim 0.58$  at which the  $\alpha$  phase entirely disappears. The initial volume of the Pd structure  
55 expands by about 10% when the H/Pd ratio reaches a value close to 0.5. This dilatation can  
56 generate extremely large overall compressive stresses if the deformation is impeded by a  
57 mechanical constraint, such as in the case of a film lying on a thick substrate. If the hydrided  
58 material is unconstrained, large local stress variations can also take place if the  
59 transformation does not occur homogeneously as a result of the diffusion process. The large  
60 local or overall stress levels can induce severe local or global plastic deformation,  
61 respectively<sup>2,4,6-11</sup>. Hence, it can be expected that the hydriding-induced defects could play a  
62 pivotal role in dictating the elementary deformation/failure mechanisms and the mechanical  
63 response of the films when subjected to external mechanical loadings.

64

65 In the literature, numerous experimental works have been dedicated to the study of the  
66 effect of hydrogen on the microstructure and mechanical properties of bulk coarse-grained  
67 materials<sup>5,11-16</sup>. However, although nc materials are often considered as promising systems  
68 with demonstrated or potential ultra-high structural performances, in-depth experimental  
69 investigations on the impact of hydrogen on the mechanical behavior and the small-scale  
70 plasticity mechanisms can hardly be found in the literature. Because of the complexity of the  
71 microstructure of nc metals, the small-scale plasticity mechanisms may strongly differ from  
72 coarse grained metals. Indeed, in nc metals, depending on the grain size and the local stress  
73 state, the nucleation of leading partial dislocations from GBs or the production of  
74 deformation twins can be favored over the formation of full lattice dislocations even in  
75 metals with a high stacking fault energy (SFE)<sup>17</sup>. Furthermore, GB processes such as grain  
76 growth, GB sliding and grain rotation can be easily activated at room temperature<sup>18-20</sup>.

77

78 Very recently, Amin-Ahmadi *et al.* performed extensive TEM characterizations of the  
79 nanoscale defect mechanisms activated during hydriding/dehydriding cycles in sputtered  
80 nanocrystalline Pd films<sup>3</sup>. The results have shown that, despite the small grain size, local  
81 plasticity was mainly controlled by dislocation activity in Pd films hydrided to the  $\beta$ -phase.  
82 No clear changes of the grain size distribution and of the crystallographic texture have been  
83 observed. Surprisingly, a high density of Shockley partial dislocations (SPDs) and stacking  
84 faults (SFs) has been observed after dehydriding, indicating that the presence of hydrogen  
85 leads to a decrease of the nucleation energy barriers of SPDs which was confirmed using ab-  
86 initio calculations<sup>3</sup>. Defects observed after dehydriding involved wide SFs connected to grain  
87 boundaries and delimited by leading SPDs, narrowly dissociated dislocations involving  
88 leading and trailing SPDs as well as nanosized shear type glissile SF loops. Their presence in  
89 such a high SFE metal after dehydriding was attributed to large internal stress  
90 heterogeneities, typical of nc materials<sup>3</sup>, or to the presence of neighboring defects. The  
91 presence of residual hydrogen atoms at the SPDs core or SFs, which can stabilize these

92 defects after dehydriding, was excluded based on spatially resolved EELS measurements. No  
93 residual hydrogen atoms were detected on grain boundaries after dehydriding. In  
94 continuation of the work of Amin-Ahmadi *et al.*<sup>3</sup>, the present study is focusing on the effect  
95 of the hydriding induced SFs and SPDs on the nanoscale plasticity mechanisms and  
96 mechanical behavior of thin nanocrystalline Pd films. More precisely, Pd films subjected to a  
97 hydriding/dehydriding cycle to the  $\beta$ -phase were characterized using nanoindentation and  
98 advanced TEM techniques including in-situ high resolution TEM nanomechanical testing and  
99 automatic crystallographic orientation mapping in TEM (ACOM-TEM).

100

## 101 II. Materials and methods

102

103 Nc Pd films were sputter-deposited at room temperature on top of a Si substrate with a  
104 deposition rate of 0.3 nm/s and an Argon plasma pressure of 1.07 Pa until a thickness of 150  
105 nm was reached. Earlier work performed on these films by Amin-Ahmadi *et al.*<sup>3</sup> shows an  
106 initial microstructure with a lateral grain size of  $61 \pm 20$  nm, while texture analysis reveals a  
107 strong  $\{111\}$  preference normal to the film substrate. Hydriding/dehydriding cycles were  
108 performed in a vacuum chamber with a pressure lower than  $10^{-6}$  mbar, by instantaneously  
109 introducing an ultra-pure Ar/H<sub>2</sub> gas mixture to impose a total pressure of  $P_{H_2} = 2.3$  mbar or  
110  $P_{H_2} = 97.5$  mbar. As such, the samples were completely hydrided to either  $\alpha$  or  $\beta$  phase,  
111 respectively<sup>21</sup>. The internal stress was measured in-situ during hydriding with a high-  
112 resolution curvature measurement setup mounted on the hydriding chamber (Figure 1). The  
113 surface curvature of the cantilevered sample changes due to hydrogen-introduced  
114 expansion, which can be monitored in real time using the position of multiple laser beams  
115 reflecting off the film<sup>2</sup>. After hydriding, the gas mixture was pumped out of the chamber,  
116 resulting in a gradual decrease of the internal stress due to room temperature dehydriding  
117 (Fig. 1b). The system returns to ambient conditions. The film is then removed from the  
118 hydriding chamber. During hydrogen loading to  $\beta$  phase, the internal stress experienced by  
119 the film at equilibrium ( $\sim 920$  MPa, Fig. 1b) is significantly higher than the macroscopic yield  
120 stress of the same film ( $\sim 580$  MPa)<sup>17</sup> allowing the generation of dislocations and stacking  
121 faults<sup>3</sup>. After a few weeks, in order to study the effect of these hydriding induced defects on  
122 the hardness and Young's modulus, nanoindentation experiments were performed under  
123 atmospheric conditions on the films subjected to a complete hydriding/dehydriding cycle as  
124 well as on reference non hydride Pd films. Thus, it can be safely assumed that most or  
125 potentially all the hydrogen has left the Pd films before nanoindentation and that the  
126 internal stress induced by hydrogen loading is fully released. These measurements have  
127 been performed using the continuous stiffness mode (CSM) and the high precision DCM II  
128 head (Dynamic contact module) with a Berkovich tip mounted on an Agilent G200  
129 nanoindenter. Young's modulus and hardness of the film have been determined using the  
130 Oliver and Pharr method<sup>22</sup>. On each sample, 16 indents have been performed, and modulus  
131 and hardness values were recorded at between 10 and 15 nm depth to minimize substrate  
132 effects. Roughness measurements using a Bruker Multimode Nanoscope 8 working in  
133 medium tapping mode revealed small Rq ( $\sim 2$  nm).

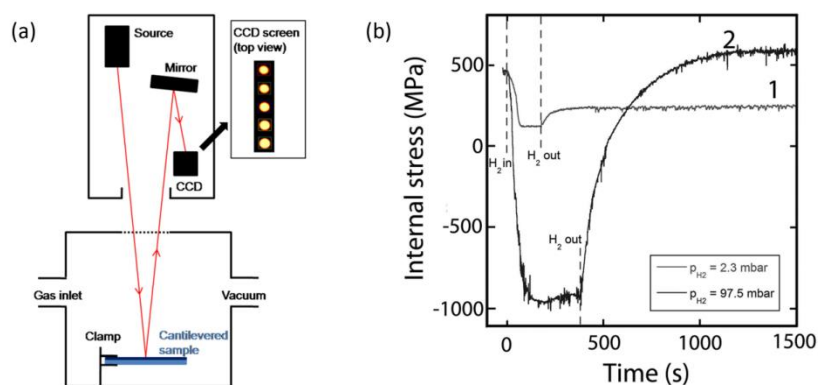
134

135 ACOM-TEM<sup>23</sup> was combined with in-situ tensile testing in order to investigate the  
136 fundamental plasticity mechanisms of as-deposited and post-mortem hydrided Pd films. In  
137 the latter, special attention was paid to the role of the pre-existing hydrogen induced SFs

138 and SPDs for the enhancement of deformation twinning. The tensile tests were performed  
 139 using the PI 95 TEM PicoIndentor instrument and the push-to-pull (PTP) device  
 140 (Bruker.Inc)<sup>24-26</sup>, see also supplementary materials. Cross-sectional TEM specimens were  
 141 prepared using focused ion beam (FIB) (“lift-out” procedure) a few weeks after the  
 142 hydriding/dehydriding cycles and mounted on the PTP. Thus, as for the nanoindentation  
 143 experiments, most or potentially even all the hydrogen has left the Pd films before in-situ  
 144 TEM straining. In order to improve the reliability of the ACOM-TEM measurements, efforts  
 145 were made to minimize the amount of overlapping grains in the tensile specimen by careful  
 146 thinning. It is also worth noting that, because the original Pd films used in the present work  
 147 are not freestanding, cross-sectional samples cut by FIB and transferred onto the PTP device  
 148 include the FIB deposited Pt protective top layer and a part of the Si-substrate (see  
 149 supplementary materials). Attempts to remove the Pt top layer and the Si bottom layer by  
 150 FIB resulted in strongly damaged Pd films. Because of the presence of these extra layers, the  
 151 present work will thus focus on the deformation mechanisms activated in the Pd films rather  
 152 than interpreting the relationship between these mechanisms and the in-situ measured  
 153 load-displacement data.

154  
 155 ACOM-TEM was performed in a FEI Tecnai G2 microscope (FEG, 200 kV), equipped with the  
 156 ASTAR system from Nanomegas. The electron probe size was  $\sim 1.5$  nm. Electron precession  
 157 with an angle of  $0.4^\circ$  was used to minimize dynamical effects and facilitate the automatic  
 158 indexing of the diffraction patterns<sup>27</sup>. Post-treatment of the data including noise  
 159 reduction, statistical analysis and interface mapping was achieved with the orientation  
 160 imaging microscopy (OIM) analysis software from EDAX. A standard EBSD cleanup procedure  
 161 is applied to this data to correct non-indexed or mis-indexed points. Furthermore, grains  
 162 with a low reliability ( $<10\%$ ) and smaller than 15 pixels were removed from the analysis.  
 163 Finally, in-situ high resolution TEM (HRTEM) tests using the PI 95 TEM PicoIndentor and the  
 164 PTP were performed in a FEI Osiris microscope (FEG, 200 kV) in order to observe in-situ  
 165 individual dislocation behavior at the nanoscale.

166



167  
 168

169 Figure 1: (a) High-resolution in-situ curvature measurement set-up mounted on a hydriding  
 170 chamber and (b) Typical internal stress evolution during hydriding to  $\alpha$  (2.3 mbar) and  $\beta$ -  
 171 phase (97.5 mbar).

172

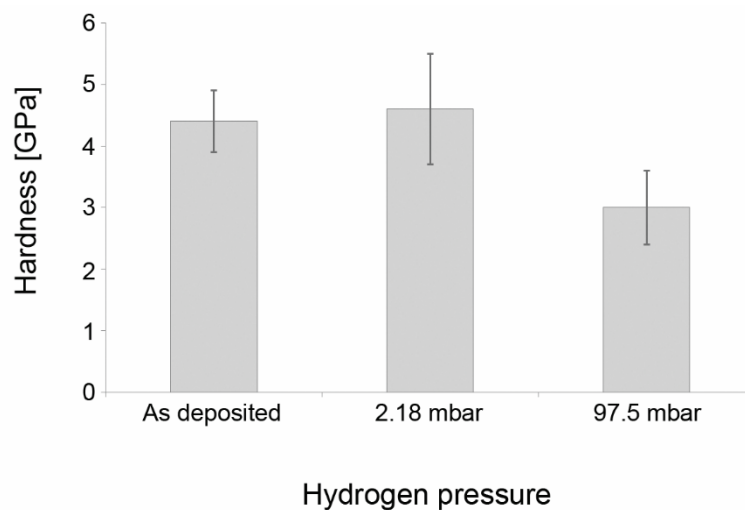
### 173 III. Results and discussion

174

#### 175 1. Nanoindentation

176

177 The effect of hydrogen charging on the mechanical response of the Pd films has been  
178 quantified by nanoindentation. The bar chart of Figure 2 compares the hardness of the as-  
179 deposited Pd film as well as of films hydrided at 2.18 mbar ( $\alpha$ -phase) and 97.5 mbar ( $\beta$ -  
180 phase), see supplementary materials for hardness-displacement curves. The hydrogen  
181 loading to the  $\beta$ -phase induces a significant softening compared to the as-deposited film  
182 while no difference is observed for a film hydrided to  $\alpha$ -phase. As mentioned in the  
183 introduction, TEM observations made by Amin-Ahmadi *et al.*<sup>3</sup> revealed a clear increase of  
184 the dislocation density and the presence of SFs and SPDs in films hydrided to  $\beta$ -phase while  
185 significant changes of the microstructure were not detected in films hydrided to  $\alpha$ -phase.  
186 The following section will thus focus on the TEM investigation of the deformation  
187 mechanisms activated in as-deposited and  $\beta$ -hydrided films. The Young's modulus of the as-  
188 deposited (resp.  $\beta$ -hydrided) film estimated by nanoindentation is equal to  $98\pm 10$  GPa (resp.  
189  $83\pm 9$  GPa).  
190



191

192 Figure 2: Hardness measurements by nanoindentation in as-deposited films, films hydrided  
193 at 2.18 mbar ( $\alpha$  phase) and at 97.5 mbar ( $\beta$  phase).

194

#### 195 2. In-situ ACOM-TEM mechanical testing

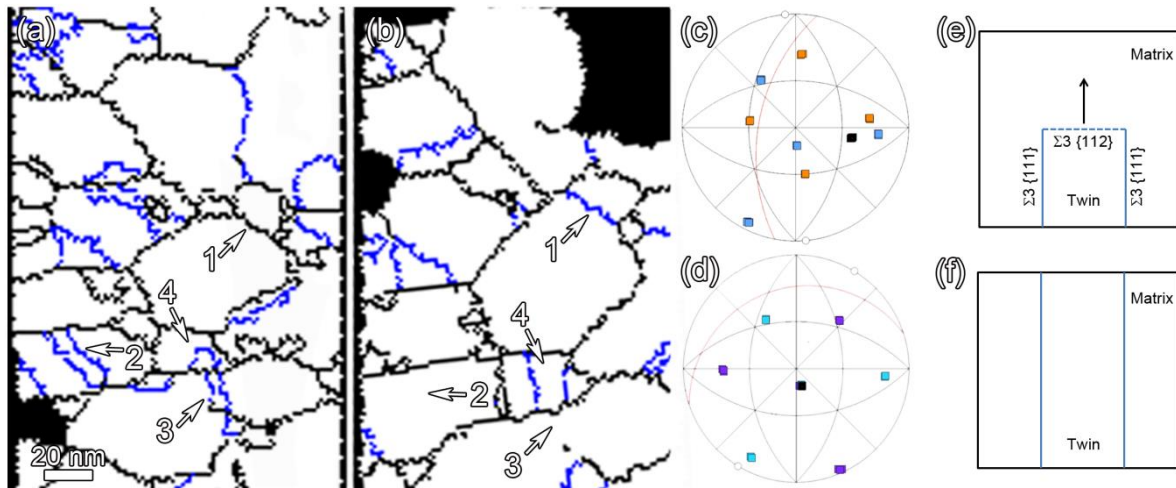
196

197 Figure 3a and Figure 3b show ACOM-TEM maps of  $\Sigma 3$  twin boundaries (TBs) in a  $\beta$ -hydrided  
198 film respectively before deformation and after an in-situ TEM tensile loading-unloading cycle  
199 up to 30  $\mu$ N. The deformation was performed in the load-control mode with a loading rate of  
200 0.5  $\mu$ N/s. Index 1 in Figure 3a and Figure 3b indicates the transformation of a GB into a TB  
201 which can be explained by grain rotation. This can be concluded both from the change of  
202 misorientation angle from 35° to 56° and from the change observed in the inverse pole  
203 figures (see Figure 3c and Figure 3d), where, after deformation, a common plane exists  
204 between a pair of {111} reflections of the two grains. The combination of this common plane  
205 and of a misorientation angle of  $60^\circ \pm 9^\circ$  is maintained for all TBs recognized with ACOM-TEM,  
206 following the Brandon criteria for  $\Sigma 3$  {111} CSL boundaries<sup>28,29</sup>. In the literature, nc fcc metals

207 with a medium to high SFE tend to deform by twinning<sup>30</sup>. GBs could transform into TBs by  
208 grain rotation in order to minimize their interfacial energy. Indeed, Olmsted *et al.* have  
209 shown using atomistic simulations on Ni that  $\Sigma 3$  boundaries tend to have a smaller energy in  
210 comparison to other GB types<sup>31</sup>. In the present work, grain rotation induced twinning can be  
211 enhanced by local changes of the GB structure due to the accumulation of dislocations at the  
212 GB<sup>17,32</sup>. Indeed, Amin-Ahmadi *et al.* have reported a loss of the coherency of  $\Sigma 3$  {111} CTBs in  
213 Pd films after hydriding/dehydriding cycles to  $\beta$  phase due to the storage of dislocations at  
214 these boundaries.  $\beta$  hydrides and the associated misfit dislocations are also expected to  
215 nucleate and to grow at GBs. The dislocations can be incorporated inside the GB (intrinsic GB  
216 dislocations) or accumulate near the GB forming extrinsic GB dislocations. Both features  
217 could affect the GB processes by changing its initial structure, orientation and energy.

218  
219 Indices 2 and 3 in Figure 3a and Figure 3b show the disappearance, after deformation, of  
220 nanotwins connected to GBs, leading to a bigger grain. Such behaviour can be explained by  
221 the nucleation and the glide of de-twinning dislocations with  $b=1/6 \langle 112 \rangle$  at the CTB/GB  
222 sites<sup>30,33</sup>. It has been shown by Li *et al.* using atomistic simulations on nc Cu, that below a  
223 certain twin thickness a dislocation-nucleation controlled softening mechanism occurs due  
224 to the nucleation and motion of partial dislocations parallel to the twin plane<sup>33</sup>. At index 4 in  
225 Figure 3a and Figure 3b, twin expansion due to the migration of  $\Sigma 3$ {112} incoherent TB (ITB),  
226 connecting two parallel  $\Sigma 3$ {111} coherent TB (CTB) can be clearly seen. A schematic  
227 illustration of this phenomenon is provided in Figure 3e and Figure 3f.  $\Sigma 3$  {112} ITBs can  
228 migrate under moderate applied stress, causing twin expansion<sup>4,34</sup>. Such behaviour could  
229 also explain the detwinning behaviour shown in indices 2 and 3 due to the nucleation and  
230 backward motion of  $\Sigma 3$ {112} ITBs. Indeed,  $\Sigma 3$ {112} ITBs can be formed by the dissociation of  
231 high energy GBs into  $\Sigma 3$ {111} CTB and  $\Sigma 3$ {112} ITB in order to decrease the total interfacial  
232 energy. It is important to note here that similar intense twinning/detwinning activity was not  
233 observed in as-deposited Pd films deformed in identical conditions. Such behaviour can be  
234 attributed to the microstructural changes in the  $\beta$  hydrided films including: i) changes of the  
235 structure/energy of GBs due to dislocation/GB interactions, which could lead to grain  
236 rotation induced twinning as well as the dissociation of GBs into CTBs and ITBs as shown in  
237 Figure 3. ii) the presence of the hydrogen induced SFs and SPDs that can act as preferential  
238 sites for twinning upon deformation. The latter was confirmed using in-situ HRTEM tensile  
239 testing as will be shown in the following section.

240

242  
243

244 Figure 3: TB map of the Pd film hydrided to  $\beta$  phase (a) before deformation and (b) after in-  
 245 situ loading-unloading cycle up to 30  $\mu\text{N}$ . Blue lines indicate  $\Sigma 3$  CSL twin boundaries while  
 246 the black lines highlight the position of all other possible GBs. Arrows with according  
 247 numbers were added to both figures in order to indicate changes in twinning behaviour after  
 248 deformation. (c) Pole figures from the GB marked as index 1 before deformation and (d)  
 249 after deformation. In each pole figure, the two colour codes of the squares represent the  
 250 different orientations of the neighboring grains while the black square indicates the common  
 251 plane, wherein a pair of  $\{111\}$  reflections of the two grains perfectly overlap after  
 252 deformation. (e,f) Schematic illustration of twin expansion due to the motion of  $\Sigma 3\{112\}$  ITB  
 253 in the grain with index 4, respectively.

254

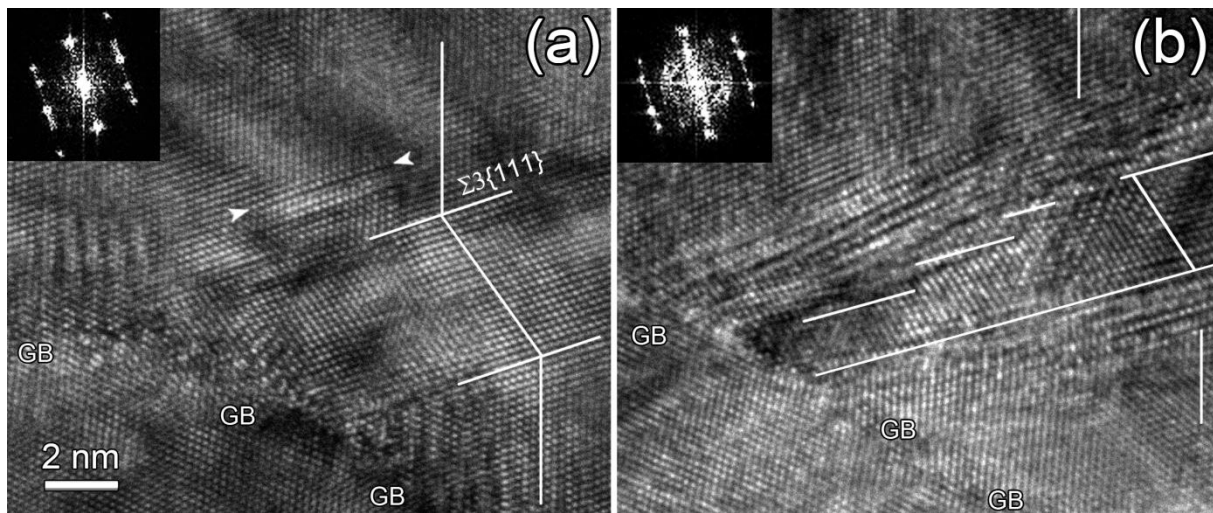
### 255 3. In-situ HRTEM mechanical testing

256

257 In Figure 4a, a growth nanotwin with two parallel CTBs connected to a GB can be observed in  
 258 the  $\beta$  (de)hydrided sample. A widely dissociated dislocation induced by hydriding to  $\beta$  phase  
 259 is indicated by white arrowheads close to the upper CTB in Figure 4a. As described in the  
 260 introduction, such wide SFs have not been observed by Amin-Ahmadi *et al.* in as-deposited  
 261 Pd films<sup>3</sup>. SFs were neither observed in Pd films hydrided to  $\alpha$  phase (low H pressure)<sup>3</sup> which  
 262 has been attributed to the small amount of hydrogen incorporated in the lattice and the low  
 263 stress levels reached during this hydriding cycle (Figure 1b). During the in-situ tensile  
 264 straining, SFs were observed to form at the CTBs (Figure 4b). This leads to a decrease of the  
 265 thickness of the twin (i.e., detwinning) as can be seen in the same figure. CTB migration  
 266 involving the nucleation and glide of new twinning dislocations at the CTB/GB intersection  
 267 sites has been reported before<sup>30,33</sup>. Such behaviour can be enhanced in the present work  
 268 due to the storage of dislocations at GBs during hydriding to  $\beta$  phase as well as the presence  
 269 of pre-existing hydrogen induced SFs (Figure 4a) that can act as preferential sites for the  
 270 nucleation of new SFs as will be seen below.

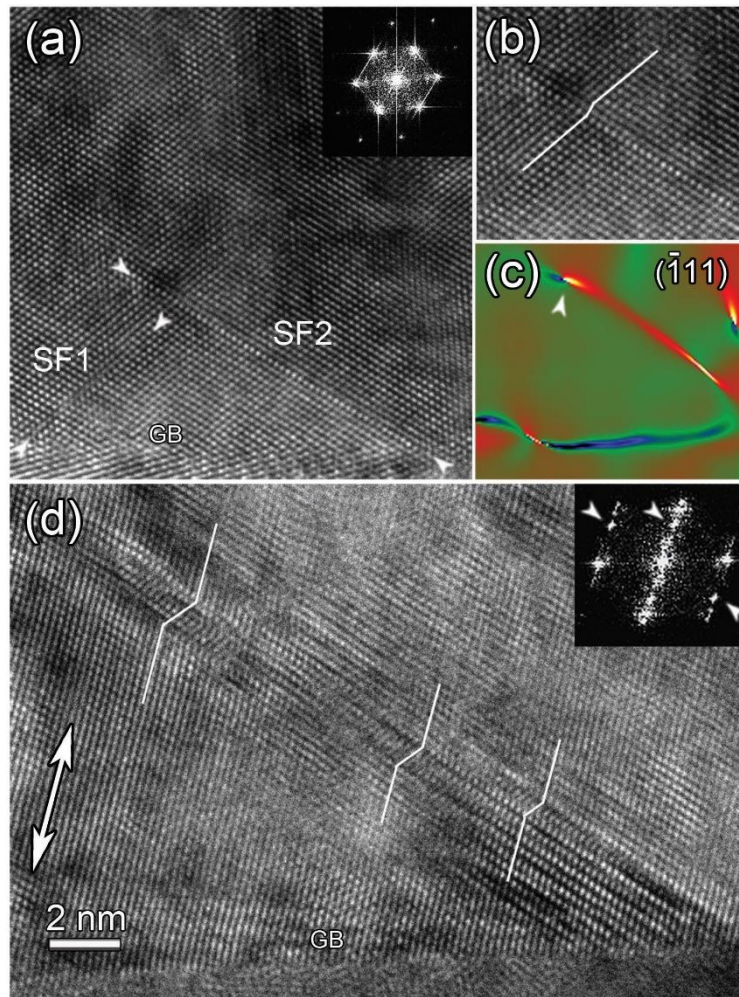
271





272  
 273 Figure 4: HRTEM images of the  $\beta$  (de)hydrided Pd film (a) before deformation and (b) after  
 274 the tensile cycle up to 160  $\mu\text{N}$ . A widely dissociated dislocation with a central SF and induced  
 275 by hydriding to  $\beta$  phase is highlighted with white arrowheads in (a) while the FFT of both  
 276 images is provided in their respective top left corner.

277 The HRTEM image of Figure 5a shows two stacking faults (SF1 and SF2) connected to a GB in  
 278 the Pd film hydrided to  $\beta$  phase, before deformation. Figure 5b exhibits the change of the  
 279 stacking sequence of the  $\{111\}$  planes due to the presence of the single SF2 while Figure 5c  
 280 exhibits a local g-map showing the position of the leading partial dislocation delimiting this  
 281 SF. The HRTEM image of Figure 5d was acquired after a loading-unloading cycle up to 160 $\mu\text{N}$ .  
 282 It shows that SF1 has disappeared due to the backward motion of the SPD delimiting this SF  
 283 towards the GB. However, SF2 transformed into a nanotwin as confirmed by the FFT  
 284 displayed in the top right inset of the same figure. This is obtained by the successive  
 285 formation of new twinning dislocations from the GB/SF interaction site. The difference  
 286 between the behaviour of SF1 and SF2 is probably due to the different sign of their Burgers  
 287 vectors with respect to the external applied stress. Using atomistic simulations Stukowski *et*  
 288 *al.* reported that in pure Pd with pre-existing SFs softening occurs due to the nucleation of  
 289 new partial dislocations parallel to the SF plane<sup>35</sup>. The presence of a SF decreases the energy  
 290 barrier for twinning by facilitating the formation of a second SF in the plane immediately  
 291 adjacent to the first SF. It is also worth noting that, although the observations shown in  
 292 Figure 5 have been performed in a single grain, the effect of the hydrogen induced SFs and  
 293 SPDs on twinning/detwinning is expected in all the grains since Amin-Ahmadi *et al.* reported  
 294 a high density of these defects homogeneously distributed within all the analyzed grains.  
 295



296  
 297 Figure 5: (a) SFs (1, 2) formed close to a GB and indicated by arrowheads. The FFT is shown in  
 298 the inset. (b) Enlarged image of SF2 in (a), (c) local g-map of the  $(\bar{1}11)$  plane with an  
 299 arrowhead indicating the position of the SPD delimiting SF2 as a hot spot. (d) Deformation  
 300 twin formed from SF2 after the loading/unloading cycles up to  $160\mu\text{N}$ . Extra twinning  
 301 reflections are highlighted with arrowheads in the FFT shown in the inset. The tensile axis is  
 302 indicated by the double arrow in (d). The white lines in (d) indicate changes of the stacking  
 303 sequence of the  $(\bar{1}11)$  plane due to the presence of twinning dislocations.

304 The results of the in-situ ACOM-TEM and HRTEM analysis confirm that SFs and SPDs induced  
 305 by hydriding to  $\beta$  phase could play an important role in the plasticity by acting as sources not  
 306 only for deformation twinning (Figure 5) but also for detwinning (Figure 4). This also explains  
 307 the softening behaviour observed in Figure 2. Indeed, several experimental investigations  
 308 and simulations have attributed mechanical softening in nc materials to twinning and partial  
 309 dislocation dominated plasticity<sup>33,35</sup>. Very recently, Y. Zhao *et al.* investigated the effect of  
 310 hydrogen charging on the plastic deformation of nc Ni using nanoindentation<sup>36</sup>. The results  
 311 revealed an hydrogen-induced softening behaviour that was explained by hydrogen-  
 312 enhanced activity of partial dislocations emitted from GBs and/or abundant hydrogen-  
 313 vacancy cluster formation around GBs. However, nanoscale characterizations of the  
 314 deformed microstructure were not performed to validate such features. The present work  
 315 thus provides first of kind experimental evidences on the role of partial dislocations in  
 316 softening of hydrided nc metallic films. Hydrogen-vacancy cluster formation around GBs can  
 317 be excluded based on the earlier spatially resolved EELS measurements performed on GBs

318 and dislocations by Amin-Ahmadi *et al.* Since the absence of residual hydrogen atoms at the  
319 defects has been confirmed based on EELS<sup>3</sup>, a possible impact on the small-scale plasticity  
320 mechanisms observed with in-situ TEM can be excluded. However, its contribution to the  
321 softening behavior observed in nanoindentation experiments cannot be totally excluded as  
322 these measurements have been performed on samples not affected by the FIB or electron  
323 exposure.  
324

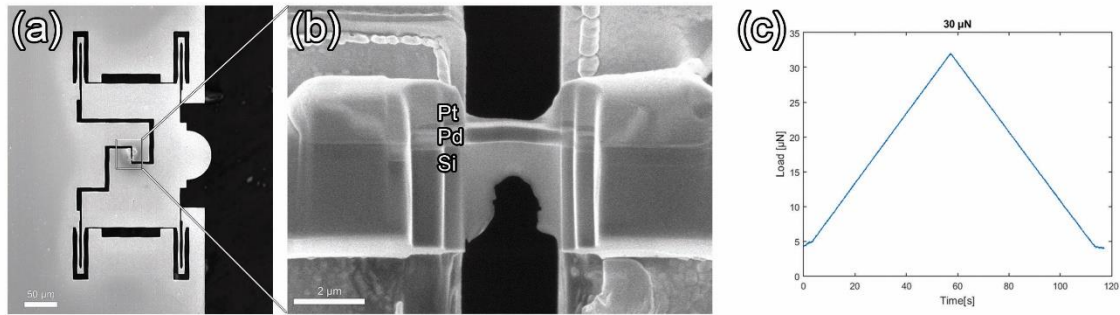
#### 325 IV. Conclusions

326  
327 The effect of SPDs and SFs induced by hydriding/dehydriding cycles to  $\beta$  phase on the  
328 mechanical response and the nanoscale plasticity mechanisms in nc thin Pd films has been  
329 investigated using nanoindentation and in-situ TEM nanomechanical testing. The in-situ  
330 HRTEM observations revealed that the pre-existing SFs act as preferential sites for  
331 twinning/detwinning in agreement with the in-situ ACOM-TEM observations. The latter also  
332 revealed the activation of grain rotation induced twinning and the dissociation of GBs into  
333  $\Sigma\{111\}$  CTB and  $\Sigma\{112\}$  ITB followed by the migration of the ITBs. Such features were  
334 attributed to changes of the local structure/energy of GBs after hydrogen loading due to the  
335 storage of dislocations at GBs. The origin of these dislocations can be attributed to the  
336 nucleation of dislocations from GBs or intra-granular sources (due to the build-up of the  
337 internal stress during  $\beta$  hydriding) as well as the preferential formation of the  $\beta$  hydrides and  
338 the resulting misfit dislocations on GBs. The observed partial dislocation dominated plasticity  
339 and GB processes could explain the softening observed in the  $\beta$  hydrided films compared to  
340 the as-deposited films, as revealed by nanoindentation.  
341

#### 342 V. Supplementary Material

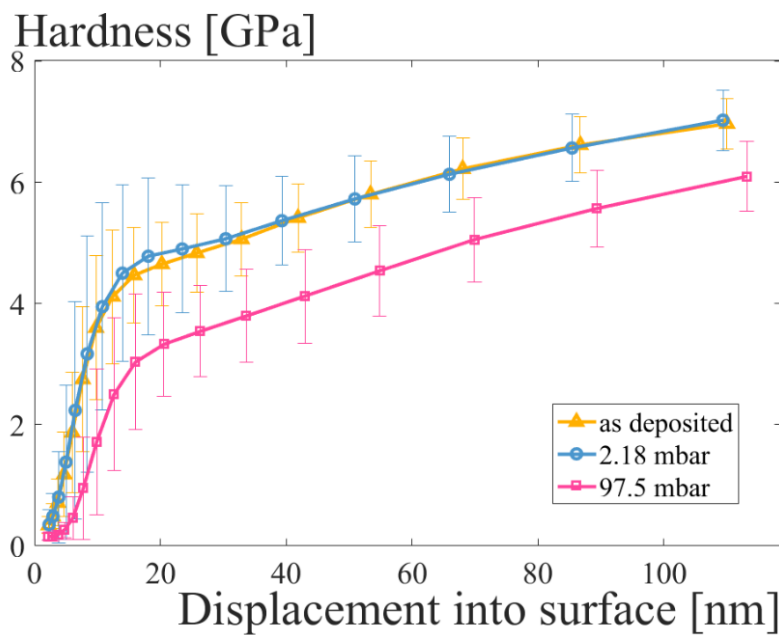
343  
344 The PI 95 TEM PicoIndenter holder from Bruker Inc. with a conductive diamond flat punch  
345 indenter was used to perform load-controlled compression. To convert the compressive  
346 force to a tensile force, the sample was mounted on a push-to-pull (PTP) chip (Figure S1a).  
347 This device is a special microelectromechanical system which contains four identical springs  
348 mounted in the corners of the system and arranged parallel to the indentation direction. The  
349 diamond tip compresses the semicircular end of the PTP device, inducing a uniaxial tensile  
350 loading over the middle gap of the PTP device. In this experiment, the stiffness of the springs  
351 was equal to 450 N/m.

352 For sample preparation, a FEI Helios dual beam FIB/SEM instrument was used to cut the Pd  
353 thin film as cross-sectional samples, including the FIB deposited Pt protective layer and a  
354 part of the Si substrate. Using a build-in Omniprobe micromanipulator, the sample was  
355 transferred to the middle gap of the PTP device (Figure S1b) and attached with electron-  
356 beam deposited Pt. Thus, in order to obtain thin Pd samples for ACOM and HRTEM, careful  
357 thinning was performed with FIB on the PTP. Figure S1c shows an example of a loading-  
358 unloading cycle up to 30  $\mu$ N during the in-situ experiment.  
359



360  
 361 Figure S1: (a) Low magnification SEM image of the PTP chip. The FIB sample is mounted over  
 362 the highlighted middle gap and shown in (b) at a higher magnification. (c) Load-unloading  
 363 cycle up to 30  $\mu\text{N}$ .

364 Usual rule of thumbs in nanoindentation testing suggests that for a reliable measurement,  
 365 roughness should represent less than 5 % of the indentation depth. Here, the hardness values are  
 366 taken between 10 and 12% of the film thickness in order to avoid substrate effect, i.e. between 15  
 367 and 18 nm, which is a little less than the above-mentioned rule. Nevertheless, roughness mainly  
 368 induces scatter in the measurements, which is taken into account by the confidence interval. The  
 369 additional figure provided as supplementary material (figure S2) shows that the conclusions are  
 370 still valid despite of the larger scatter. Moreover, the relative position of the hardness values of  
 371 the different samples does not change even if the hardness is considered at larger depths so as to  
 372 fulfil the rule indicated above.  
 373



374  
 375 Figure S2: Hardness-displacement curves of the nanoindentation experiments performed under  
 376 atmospheric conditions on the films subjected to a complete hydriding/dehydriding cycle as well  
 377 as on reference non hydride Pd films.  
 378  
 379

380 **Acknowledgements**

381

382 This work was supported by the Hercules Foundation under Grant AUHA13009; the Flemish  
383 Research Fund (FWO) under Grant G.0365.15N; and the Flemish Strategic Initiative for  
384 Materials (SIM) under the project *InterPoCo*. Dr. H. Idrissi is mandated by the Belgian  
385 National Fund for Scientific Research (FSR-FNRS). We would like to thank dr. Hadi Pirgazi  
386 from UGent for his technical support to process the ACOM data in the OIM Analysis  
387 software.

388

389 **References**

390

391 1. K.L. Salcedo, C.A. Rodríguez, F.A. Perez and H. Riascos, J. Phys. Conf. Ser. **274**, (2011).

392

393 2. R. Delmelle, G. Bamba and J. Proost, Int. J. Hydrogen Energy **35**, 9888 (2010).

394

395 3. B. Amin-Ahmadi, D. Connétable, M. Fivel, D. Tanguy, R. Delmelle, S. Turner, L. Malet,  
396 S. Godet, T. Pardoën, J. Proost, D. Schryvers and H. Idrissi, Acta Mater. **111**, 253  
397 (2016).

398

399 4. B. Amin-Ahmadi, H. Idrissi, R. Delmelle, T. Pardoën, J. Proost and D. Schryvers, Appl.  
400 Phys. Lett. **102**, 071911 (2013).

401

402 5. V. Bérube, G. Radtke, M. Dresselhaus and G. Chen, Int. J. energy Res. **31**, 637 (2007).

403

404 6. H. Kou, J. Lu and Y. Li, Adv. Mater. **26**, 5518 (2016).

405

406 7. E.M. Salomons, R. Feenstra, D.G. De Groot, J.H. Rector and R. Griessen, J. Less-  
407 Common Met. **130**, 415 (1987).

408

409 8. H. Gleiter, Adv. Mater. **4**, 474 (1992).

410

411 9. M.V. Goltsova and G.I. Zhironov, Met. Sci. Heat Treat. **49**, 141 (2007).

412

413 10. T.B. Flanagan and W.A. Oates, Annu. Rev. Mater. Sci. **21**, 269 (1991).

414

415 11. R. Delmelle, B. Amin-Ahmadi, M. Sinnaeve, H. Idrissi, T. Pardoën, D. Schryvers and J.  
416 Proost, Int. J. Hydrogen Energy **40**, 7335 (2015).

417

418 12. J.M. Wheeler and T.W. Clyne, Int. J. Hydrogen Energy **37**, 14315 (2012).

419

420 13. E. Dillon, G. Jimenez, A. Davie, J. Bulak, S. Nesbit, A. Craft, Mater. Sci. Eng. A **524**, 89  
421 (2009).

422

423 14. M.V. Goltsova, Y.A. Artemenko and V.I. Zaitsev, J. Alloys Compd. **293**, 379 (1999).

424

- 425 15. G. Jimenez, E. Dillon, R. Miller, F. Massicotte, S. Nesbit and A. Craft, *Scr. Mater.* **59**,  
426 870 (2008).  
427
- 428 16. G. Jimenez, E. Dillon, J. Dahlmeyer, T. Garrison, T. Garrison, S. Darkey, K. Wald, J.  
429 Kubik, D. Paciulli, M. Talukder, J. Nott, M. Ferrer, J. Prinke, P. Villaneuva, F. Massicotte,  
430 K. Rebeiz, S. Nesbit, and A. Craft, *Adv. Chem. Eng. Sci.* **6**, 246 (2016).  
431
- 432 17. B. Wang, H. Idrissi, M. Galceran, M.S. Colla, S. Turner, S. Hui, J.P. Raskin, T. Pardoën, S.  
433 Godet and D. Schryvers, *Int. J. Plast.* **37**, 140 (2012).  
434
- 435 18. A. Kobler, J. Lohmiller, J. Schäfer, M. Kerber, A. Castrup, A. Kashiwar, P.A. Gruber, K.  
436 Albe, H. Hahn and C. Kübel, *Beilstein J. Nanotechnol.* **4**, 554 (2013).  
437
- 438 19. F. Mompiau and M. Legros, *Scr. Mater.* **99**, 5 (2015).  
439
- 440 20. Y. Ivanisenko, N.A. Enikeev, K. Yang, A. Smoliakov, V.P. Soloviev, H. Fecht and H. Hahn,  
441 *Mater. Sci. Eng. A* **668**, 255 (2016).  
442
- 443 21. R. Delmelle, S. Michotte, M. Sinnaeve and J. Proost, *Acta Mater.* **61**, 2320 (2013).  
444
- 445 22. W.C. Oliver, and G.M. Pharr, *J. Mater. Res.* **19**, 3 (2004).  
446
- 447 23. E.F. Rauch and M. Véron, *Mater. Charact.* **98**, 1 (2014).  
448
- 449 24. A. Kobler, A. Kashiwar, H. Hahn and C. Kübel, *Ultramicroscopy* **128**, 68 (2013).  
450
- 451 25. H. Idrissi, C. Bollinger, F. Boioli, D. Schryvers and P. Cordier, *Sci. Adv.* **2**, 1 (2016).  
452
- 453 26. H. Idrissi, A. Kobler, B. Amin-ahmadi, M. Coulombier, M. Galceran, J.P. Raskin, S.  
454 Godet, C. Kübel, T. Pardoën and D. Schryvers, *Appl. Phys. Lett.* **104**, 101903 (2014).  
455
- 456 27. A. Kobler and C. Kübel, *Ultramicroscopy* **173**, 84 (2017).  
457
- 458 28. D.G. Brandon, *Acta Metall.* **14**, 1479 (1966).  
459
- 460 29. A.F. Acton and M. Bevis, *Acta Crystallogr. Sect. A* **27**, 175 (1971).  
461
- 462 30. Y.T. Zhu, X.Z. Liao and X.L. Wu, *Prog. Mater. Sci.* **57**, 1 (2012).  
463
- 464 31. D.L. Olmsted, S.M. Foiles and E.A. Holm, *Acta Mater.* **57**, 3694 (2009).  
465
- 466 32. H. Idrissi, B. Wang, M.S. Colla, J.P. Raskin, D. Schryvers and T. Pardoën, *Adv. Mater.* **23**,  
467 2119 (2011).  
468
- 469 33. X. Li, Y. Wei, L. Lu, K. Lu and H. Gao, *Nature* **464**, 25 (2010).  
470
- 471 34. H. Idrissi, B. Amin-Ahmadi, B. Wang and D. Schryvers, *Phys. Status Solidi Basic Res.*

- 472           **251**, 1111 (2014).  
473  
474   35.   A. Stukowski, K. Albe and D. Farkas, Phys. Rev. B - Condens. Matter Mater. Phys. **82**, 1  
475           (2010).  
476  
477   36.   Y. Zhao, M.Y. Seok, D.H. Lee, J.A. Lee, J.Y. Suh, and J.I. Jang, Philos. Mag. **96**, 3442–  
478           3450 (2016).  
479